ANALYSIS OF TOPOGRAPHIC EFFECTS OBSERVED IN SPECTRAL FEATURES EXTRACTED FROM CHANDRAYAAN-1 M3 IMAGERY. A. Grumpe[1], F. Brinkmeier[1], C. Wöhler[1,2]. [1]Image Analysis Group, Dortmund University of Technology, D-44221 Dortmund, Germany; {arne.grumpe | felix.brinkmeier | christian.woehler}@tu-dortmund.de; [2]Geologic Lunar Research (GLR) Group

Introduction: The elemental composition of lunar iron bearing minerals causes specific shapes of the observed reflectance spectrum R_λ. Conversely, the elemental composition of the surface is expressed by distinct features of the reflectance spectrum [1]. The spectral features examined in this analysis are the absorption wavelength, full width at half maximum (FWHM), absorption depth, and integrated band depth (IBD) of the ferrous absorption trough at ~1000 nm (all of which are computed after continuum removal), as well as the hydroxyl absorption at ~3000 nm. The absorption wavelength λ_{abs} allows to distinguish between high-Ca and low-Ca pyroxene and Mg-rich rock such as norite. The relative absorption depth δ is related to the abundance of mafic minerals and also to the optical maturity of the soil. An increased value of the FWHM *W* of the absorption trough indicates the presence of olivine [2, 3]. The IBD of the ferrous absorption trough at ~1000 nm is also correlated with the abundance of mafic minerals [4]. The hydroxyl absorption at ~3000 nm identified in [5] can be represented by the spectral ratio R_{2896}/R_{2697}.

General approach: Topographic effects on the spectral features are examined using the M^3 data set, which is available through the Planetary Data System (PDS) as absolute radiance images [6]. We applied a thermal correction to the radiance spectra by modeling them as being composed of a scaled standard lunar reflectance spectrum and a black body emission spectrum in the wavelength range 2377–2936 nm, thus estimating the temperature of the black body. In order to determine the reflectance spectrum, we divide the radiance spectrum by the solar irradiance spectrum as defined by the American Society for Testing and Material (ASTM) [7]. The reflectance is then normalized to an incidence angle of $\vartheta_i = 30°$, an emission angle of $\vartheta_e = 0°$, and a phase angle of $\alpha = 30°$ based on the Lunar-Lambert reflectance model with the phase parameter computed according to [8]. The incidence and emission angle are determined based on the assumption of a smooth spherical surface, where deviations due to topography are neglected. The spectral features are extracted from the reflectance spectrum as described in [1].

Regression scheme: In order to determine the effect of topography, a linear regression based correction is applied to the spectral features. Let $\Delta\vartheta_i$ and $\Delta\vartheta_e$ be the deviations of the true, topography-dependent incidence and emission angle from the values obtained under the assumption of a spherical surface. We determined these deviations based on a digital elevation map (DEM) of high lateral resolution obtained with the photometric approach introduced in [9]. For all pixels associated with a low inclination angle of the surface of less than 2°, we computed the locally weighted mean of the spectral features. A local correction factor $c(\Delta\vartheta_i, \Delta\vartheta_e)$ with $c(\Delta\vartheta_i, \Delta\vartheta_e) * SF = SF_{mean}$ is computed, where SF corresponds to the pixel-specific spectral feature and SF_{mean} denotes the locally weighted mean.

An approximation $\tilde{c}(\Delta\theta_i, \Delta\theta_e)$ to the local correction factor is computed using a linear regression of the form $\tilde{c}(\Delta\vartheta_i, \Delta\vartheta_e) = (a_i + b_i\alpha)\Delta\vartheta_i + (a_e + b_e\alpha)\Delta\vartheta_e$, where a_i, b_i, a_e, and b_e are the regression parameters. The function $\tilde{c}(\Delta\theta_i, \Delta\theta_e)$ captures the topographic effects on the spectral features, which are supposed to be removed by dividing the measured features by $\tilde{c}(\Delta\theta_i, \Delta\theta_e)$. The regression parameters are determined on the area shown in Fig. 1a, displaying many topographic details. The region shown in Fig. 1b is used as a further test area.

Results: There is a clear correlation between the angular deviations $\Delta\vartheta_i$ and $\Delta\vartheta_e$ and local variations of the spectral features. Especially noteworthy are the topography dependence of the absorption wavelength λ_{abs} and the trough FWHM *W*. The observed and the topography-corrected values of λ_{abs} and *W* are shown in Figs. 2 and 3, respectively. The value of λ_{abs} is underestimated for surface parts inclined towards the sun and overestimated otherwise, which explains the observation of spurious Mg-rich rock deposits (associated with anomalously low absorption wavelengths) on crater rims inclined towards the sun in the petrographic maps in [1]. The value of *W* is overestimated for surface parts inclined away towards the sun and vice versa. For the second test area, the absorption depth δ clearly shows variations with surface details such as small craters, which are largely compensated by the regression approach (Fig. 4). For the IBD the effect is similar but less pronounced (Fig. 5).

Similarly, a dependence on topography is observed for the strength of the hydroxyl absorption indicated by the R_{2896}/R_{2697} spectral ratio (Fig. 6a). Especially, the value of R_{2896}/R_{2697} is anomalously small (i.e. the hydroxyl absorption is anomalously strong) for large surface parts inclined away from the sun. However, the

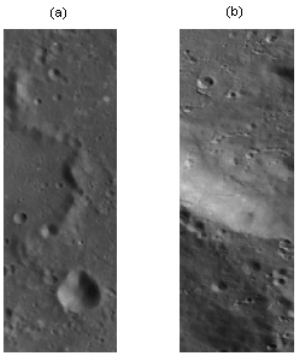

Fig. 1: (a) Region on which the regression parameters were determined (floor of Purbach crater). (b) Second test region (SW rim of Huggins crater).

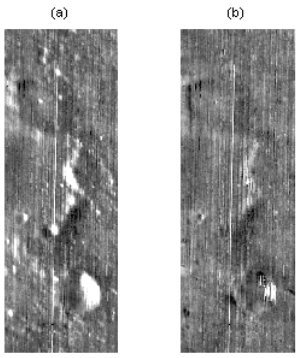

Fig. 2: Absorption wavelength λ_{abs} (a) before and (b) after correction of topography. Grey value range: 900–950 nm.

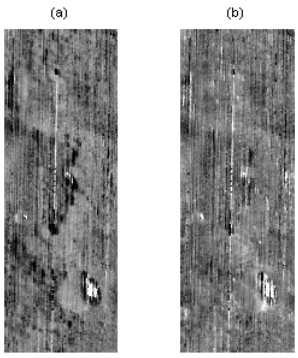

Fig. 3: FWHM *W* of the ~1000 nm absorption trough (a) before and (b) after correction of topography. Grey value range: 150–250 nm.

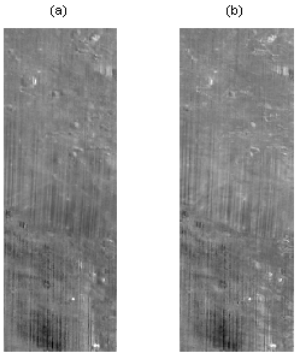

Fig. 4: Absorption depth δ (a) before and (b) after correction of topography. Grey value range: 0–0.15.

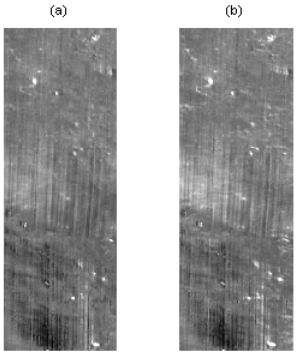

Fig. 5: IBD (a) before and (b) after correction of topography. Grey value range: 0–30.

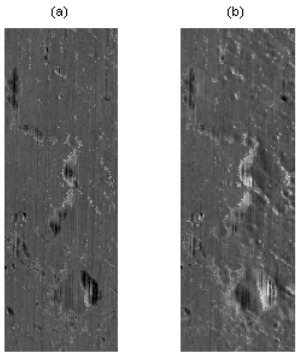

Fig. 6: R_{2900}/R_{2700} spectral ratio (a) before and (b) after correction of topography. Grey value range: 1–1.15.

topographic correction shown in Fig. 6b remains somewhat imperfect, which is due to the fact that not all surface parts inclined away from the sun show a decrease of R_{2896}/R_{2697} but some even a slight increase, e.g. in the image center (but it should be noted that the measured R_{2896}/R_{2697} values may be affected by imperfections of the thermal correction of the radiance spectra). The main factor governing the strength of the hydroxyl absorption may well be the surface temperature rather than the topography. This would be in accordance with the hypothesis that lunar hydroxyl ions originate from surface chemistry effects due to irradiation of high-energy solar wind protons on the oxygene-rich lunar surface [10], where hydroxyl ions are preferentially formed at low temperatures. A possible temperature dependence cannot be verified directly based on M^3 multispectral data as they do not allow to estimate surface temperatures below ~200 K due to the lack of spectral coverage beyond 3000 nm.

Conclusion: The topography and the resulting local variations of the illumination and observation geometry have a notable systematic effect on the spectral features. Using a DEM of high lateral resolution, we have shown that our empirical regression approach is able to perform a reasonable topography correction for the absorption wavelength, the FWHM, and the relative depth of the ~1000 nm absorption trough. The topography dependence of the hydroxyl absorption is much less clearly pronounced and may rather be a dependence on surface temperature. Future work will involve the use of physical reflectance models to explain the observed effects of topography on the spectral features.

References: [1] Wöhler C. et al. (2011) *Planetary and Space Science, 59,* 92–110; [2] Smrekar S. and Pieters C. M. (1985) *Icarus 63,* 442-452; [3] King T. V. V. and Ridley, W. I. (1987) *JGR 92,* 11457–11469; [4] Dhingra E. F. et al. (2010) *LPSC XXXXI,* Abstract #2494; [5] Clark R. et al. (2010) *LPSC XXXXI,* Abstract #2302 ; [6] http://pds.jpl.nasa.gov; [7] ASTM (2000) E-490-00; [8] McEwen A. S. (1991) *Icarus, 92*, 298-311; [9] Grumpe A., Wöhler C. (2011) *this volume*; [10] McCord T. B. et al. (2010) *LPSC XXXXI,* Abstract #1860.